Solid State Phenomena
ISSN: 1662-9779, Vol. 389, pp 51-58
doi:10.4028/p-L8oWxo

Submitted: 2026-01-19
Revised: 2026-02-23
Accepted: 2026-02-24
Online: 2026-04-16

Combined Finite Element Simulation and Regression Modeling for Predicting Final Protrusion Length of Twisted Hairpin Legs in Stators

Donghoon Han[1,a], Donghyuk Cho[1,b], Seik An[2,c] and Jeong Whan Yoon[1,3,d*]

[1]KAIST, 291 Daehak-ro, Yuseong-gu, Daejeon 34141, Republic of Korea

[2]KIA, 95, Kiajadongcha-ro, Ujeong-eup, Hwaseong-si, Gyeonggi-do, Republic of Korea

[3]School of Engineering, Deakin University, Waurn Ponds, VIC 3216, Australia

[a]dhhan218@kaist.ac.kr, [b]d.cho@kaist.ac.kr, [c]asik@kia.com, [d*]j.yoon@kaist.ac.kr

Keywords: electric motor, hairpin, finite element modeling, twisting process.

Abstract. This study presents an integrated finite element-based framework for analyzing the final protrusion length of enameled copper hairpins during stator manufacturing. Protrusion uniformity is essential for reliable laser welding, yet it is often degraded by layer-dependent deformation during expanding and twisting. To clarify the mechanisms governing protrusion variation, a bilayer material model for the copper–enamel system was developed and validated using tensile tests, indentation-based inverse characterization, and three-point bending experiments. Mechanically consistent boundary conditions for expanding and twisting were reconstructed from manufacturing observations and incorporated into FE simulations. The results indicate that twisting governs protrusion length through axial material redistribution, whereas expanding mainly serves as a feasibility-enabling step that establishes stable tool engagement. Based on these insights, a physics-guided regression formulation was introduced to relate key twisting kinematics to protrusion length. The proposed framework provides a mechanistic basis for understanding protrusion variability and supports further development toward rapid prediction and variability control.

Introduction

Hairpin stator technology has become a key enabler for high-efficiency electric motors due to its high slot fill factor and favorable thermal performance [1,2]. In hairpin stator manufacturing, the uniformity of the final protrusion length of hairpin legs is critical for reliable laser welding and overall assembly quality [3,4]. However, significant layer-to-layer protrusion variation is frequently observed after the expanding and twisting processes, leading to excessive post-cutting and increased copper waste.

Despite its practical importance, the origin of protrusion variability remains insufficiently understood. Protrusion length is influenced by multiple interacting factors, including the initial geometry of the hairpin leg, the mechanical response of the enamel-coated copper wire, and the complex kinematics of expanding and twisting [5,10,11]. In production environments, direct measurement of internal deformation and tool–hairpin interaction is not available, making it difficult to isolate dominant mechanisms through experiments alone.

To address this challenge, the present study adopts a finite element–based framework to investigate protrusion behavior during hairpin forming. A bilayer material model is developed to represent the mechanical contribution of the enamel coating [6–9], and realistic boundary conditions for expanding and twisting are reconstructed from process observations. Using FE-generated datasets from representative forming conditions, a physics-guided regression formulation is developed to provide a reduced-order description of the twisting-driven protrusion mechanism. The proposed framework aims to clarify the mechanistic origin of protrusion variability and establish a basis for further quantitative development.

This paper contributes a mechanically consistent FE framework capable of reproducing protrusion evolution under realistic forming conditions, and a mechanistic clarification that twisting governs protrusion through axial feed redistribution, whereas expanding primarily ensures stable engagement and feasible initial conditions. The framework further demonstrates that, under identical production settings across layers, final protrusion scatter is predominantly inherited from layer-dependent initial geometric offsets. These findings establish a quantitative basis for reduced-order protrusion prediction and geometry-based variability control.

Material Modeling

Accurate representation of the mechanical behavior of enameled copper hairpins is essential for predicting deformation and springback during the expanding and twisting processes. Although the enamel coating is thin, prior studies have shown that it contributes non-negligibly to bending stiffness and elastic recovery, particularly under small-radius deformation. Accordingly, a bilayer material modeling strategy-consisting of a copper core and an outer enamel coating-was adopted, following established approaches for coated conductors and hairpin components [5–9].

Uniaxial tensile tests were conducted to characterize the mechanical behavior of the copper core. To exclude the influence of the enamel coating, a 20-mm gauge section was machined from an 80-mm wire segment by locally removing the enamel, as illustrated in Fig. 1a. Because drawn copper wires can exhibit within-spool mechanical variability due to drawing history and microstructural gradients [13,14], specimens were extracted from the head, middle, and tail regions of the same spool.

Fig. 1b compares the true stress–strain responses obtained from the three locations. Only minor differences in yield stress and hardening rate were observed, indicating that the mechanical heterogeneity along the spool length is negligible for the present application. Consistent with previous observations for hairpin conductors [5], a single representative stress–strain curve was therefore adopted to define the isotropic hardening behavior of the copper core in the FE simulations. The calibrated material coefficients are summarized in Table 1.

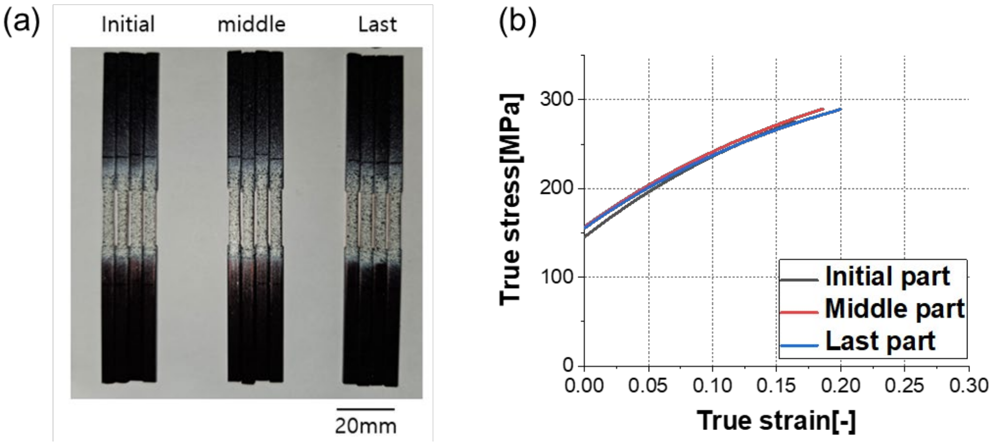

Fig. 1. (a) Uniaxial tensile test specimens. (b) Tensile test results of each sections.

Table 1. Material coefficients of hairpin copper.

$\bar{\sigma}\left(\bar{\varepsilon}^{p}\right)=a-b\exp\left(-c\bar{\varepsilon}^{p}\right)$		
a[MPa]	b[MPa]	c[-]
386.2	241	4.74

Indentation-Based Inverse Characterization of the Enamel Layer.

Direct tensile testing of the enamel coating is impractical due to its extremely small thickness. Therefore, the enamel properties were identified using an indentation-based inverse finite element approach, following methodologies established for thin coatings and layered materials [5–7,15]. An axisymmetric indentation model was employed to efficiently reproduce the experimental nano-indentation force–depth response while retaining sufficient accuracy for coating characterization.

Fig. 2 shows the axisymmetric indentation FE model and the effective indenter geometry. Prior to introducing the enamel layer, indentation simulations were first performed on bare copper to calibrate the effective indenter tip radius. As demonstrated in Fig. 3a, simulated force–depth curves obtained with different assumed tip radii were compared with experimental measurements, and the best agreement was achieved for an effective tip radius of approximately 1200 nm, consistent with values reported in the literature for calibrated or partially blunted indentation tips [5,15].

With the indenter geometry fixed, the enamel layer was reintroduced into the model for inverse material identification. Based on prior reports indicating negligible strain-hardening behavior in thin polymer-based coatings [6,7], the enamel was modeled as an elastic–perfectly plastic material. The Young's modulus was obtained directly from the unloading stiffness of the indentation experiments, while the yield strength was calibrated by matching the simulated and experimental indentation responses on the coated region. Fig. 3b illustrates the sensitivity of the simulated force–depth curves to the assumed enamel yield strength, from which a value of approximately 75 MPa was identified.

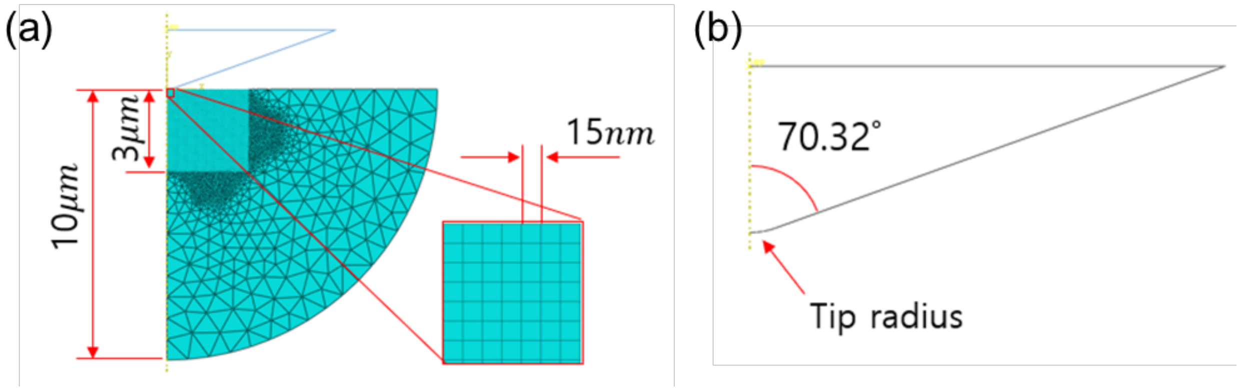

Fig. 2. Schematic of (a) nano-indentation test FE model and (b) the indenter tip radius.

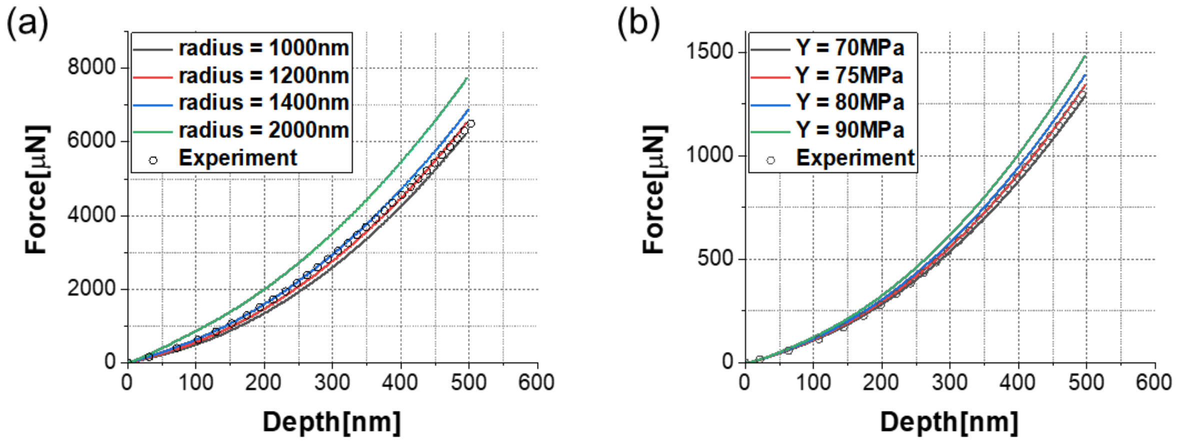

Fig. 3. (a) Reverse-engineering result of the copper indentation force–depth response for various indenter tip radii. (b)Enamel indentation force-depth response for various assumed yield stress.

Bilayer Material Model Construction.

The calibrated copper and enamel properties were combined into a three-dimensional bilayer FE model, with layer thicknesses assigned based on microscopy measurements. Eight-node reduced-integration brick elements were used for both layers, enabling explicit representation of the stiffness contribution and springback effect of the enamel coating during forming simulations.

To validate the bilayer material model under bending-dominated deformation, three-point bending tests were performed on hairpin segments. Digital Image Correlation (DIC) was used to track deformation during loading and unloading, as shown in Fig. 4, allowing direct measurement of bending and springback angles. Table 2 compares the experimentally measured angles with FE predictions. The agreement within approximately 0.2° confirms that the proposed bilayer material model reliably captures the mechanical response relevant to the expanding and twisting processes, consistent with previous validation studies on hairpin and coated-conductor components [5].

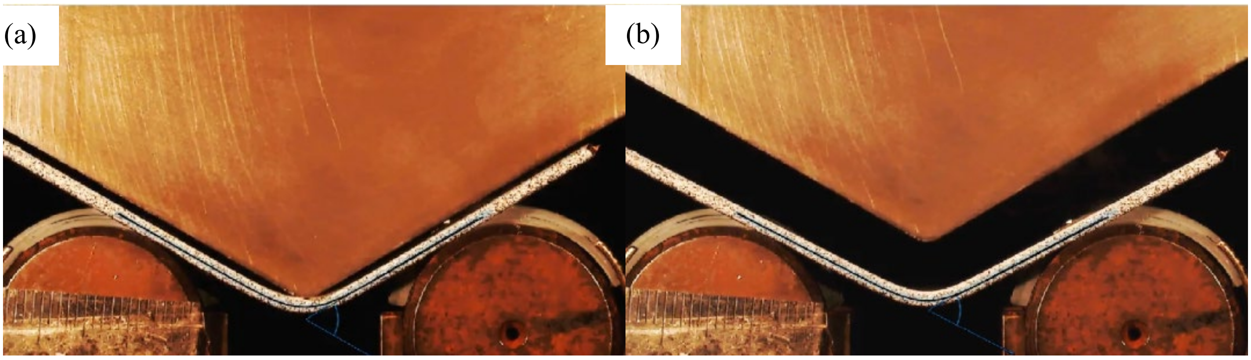

Fig. 4. DIC snapshots from the three-point bending test at the moments corresponding to (a) the bending angle and (b) the bent angle.

Table 2. Experimental and simulation comparison of three point bending test of hairpin.

Test	Bending angle[°]	Bent angle[°]	Spring-back[°]
1	60.0	54.5	5.5
2	60.2	54.7	5.5
3	59.9	54.7	5.2
Simulation	59.78	54.08	5.7

Finite Element Modeling of the Expanding and Twisting Processes

Because the production equipment does not provide direct measurements of tool positions or core motion, the boundary conditions for expanding and twisting were reconstructed from manufacturing observations and geometric measurements. To improve computational efficiency while preserving relative tool–hairpin kinematics, the reconstructed core motion was represented by equivalent prescribed tool motions in the FE model. The expanding stage was modeled only to ensure physically realistic initial conditions for twisting, as its influence on the final protrusion length was found to be weak within the feasible process window. In contrast, the twisting stage governs axial material feeding from the straight segment into the curved region and thus dominates protrusion variation; accordingly, twisting was implemented using coupled axial displacement and tool rotation reconstructed from the servo-motor logs, with a small reverse rotation applied at the end to relax torsional constraint prior to unloading.

The reconstructed expanding and twisting sequences were implemented in a rigid-tool/deformable-hairpin FE framework. To reduce numerical complexity associated with large rigid-body motion of the stator core, the core motion was kinematically replaced by equivalent prescribed tool displacements while preserving the relative tool–hairpin kinematics. The resulting deformation characteristics are illustrated in Fig. 5 and 6. During expanding, layer-dependent opening shapes appear due to differences in tool engagement depth, whereas twisting induces progressive axial feeding of the straight segment into the curved region through coupled axial–rotational motion, producing the characteristic S-shaped deformation. This mechanism directly governs the final axial protrusion length and provides the physical basis for the reduced-order predictor developed in the following section.

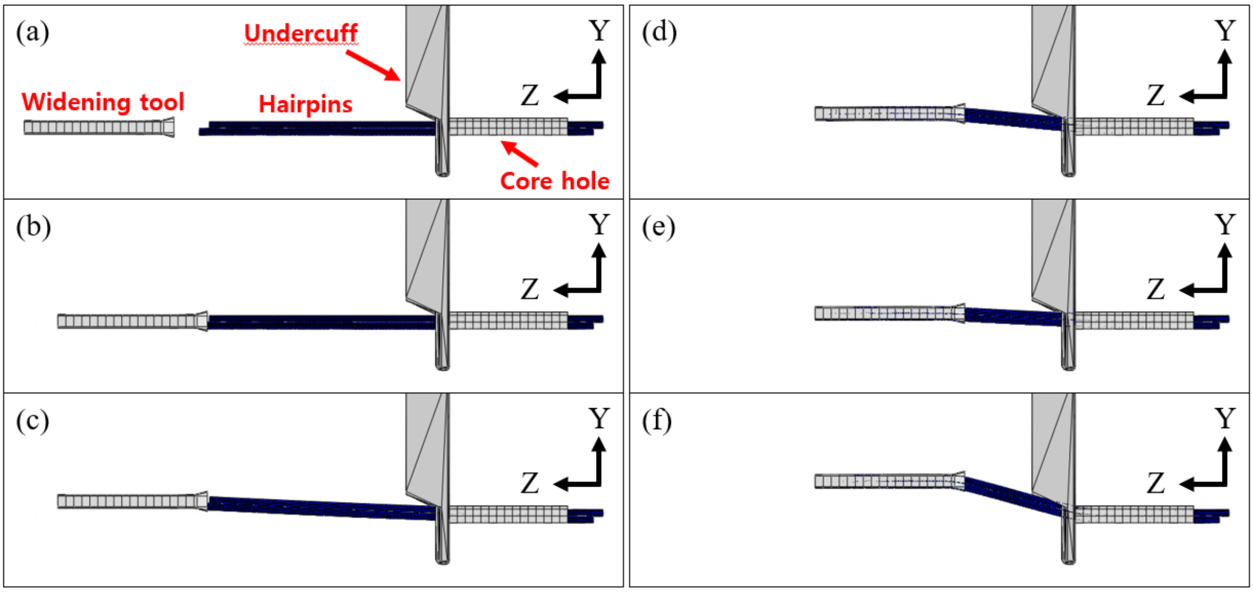

Fig. 5. FEM-based visualization of expanding processes (a) initial position of hairpins and tools (b) initial partial insertion (c) initial radial expansion (d) axial insertion (e) reverse widening and (f) final expanding.

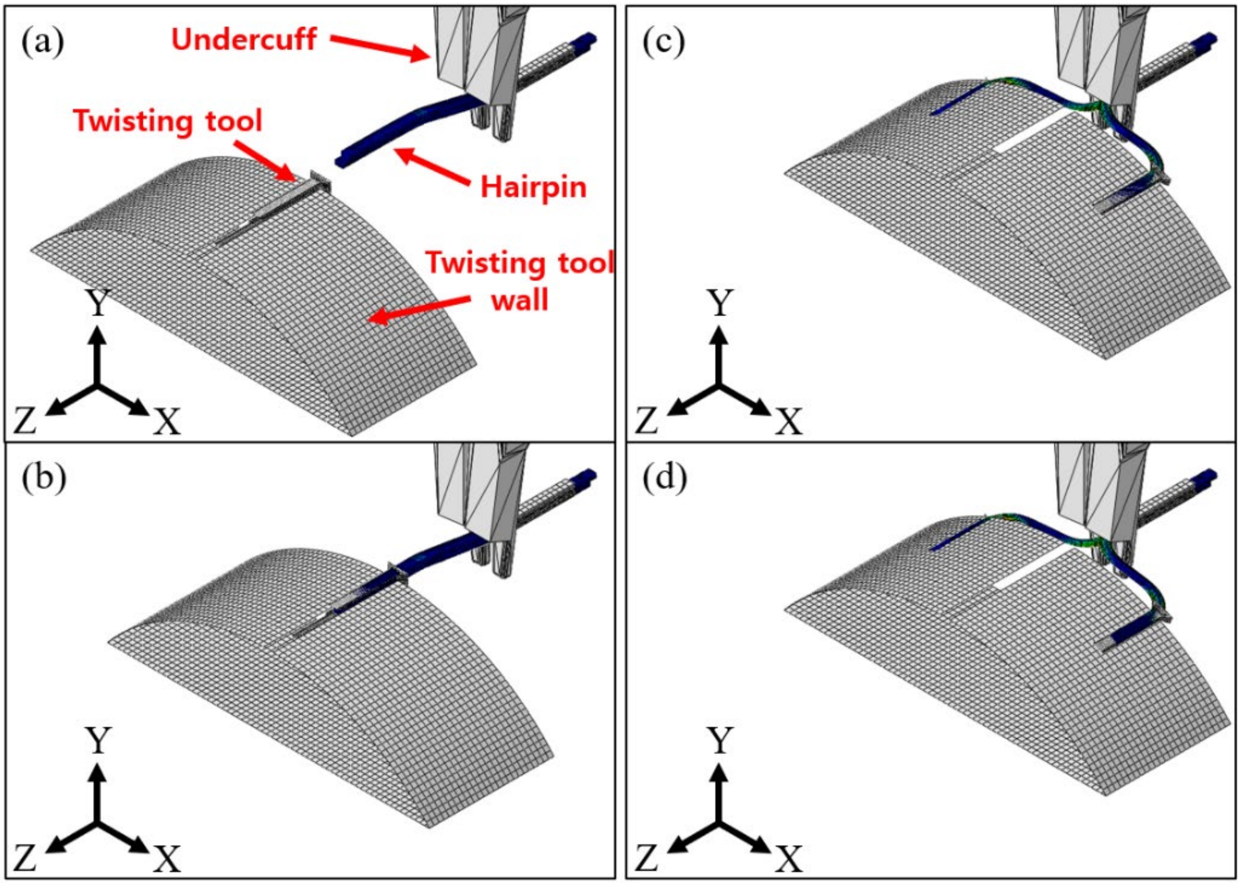

Fig. 6. FEM-based visualization of twisting processes (a) initial position of hairpins and tools (b) initial axial insertion into the twisting tool (c) further axial descent and tool rotation (d) reverse rotation.

Initial Protrusion Length Control of Hairpin Leg

Because identical twisting conditions are applied across all hairpin layers in the actual production line, twisting-related parameters cannot explain the observed layer-to-layer scatter in the final protrusion length. Instead, the dominant source of variation is the large and non-uniform initial protrusion length among layers prior to forming. Finite element simulations using the original layer-specific initial leg lengths reproduce pronounced deviations in the final protrusion, indicating that initial geometric offsets are transmitted almost directly through the expanding and twisting stages. This trend suggests an approximately one-to-one correspondence between the initial and final protrusion lengths, highlighting the role of axial material feeding during twisting as the primary mechanism governing protrusion transfer. Overall, these findings emphasize that controlling the initial protrusion length is essential for reducing layer-dependent scatter, and systematic strategies for initial-length control will be investigated in future work.

Regression Model for Predicting Final Protrusion Length

To provide a compact mathematical description of the protrusion mechanism observed in the FE simulations, a physics-guided regression formulation was introduced. The aim of this model is not to construct a fully calibrated predictor for all manufacturing conditions, but to formalize the dominant geometric relationship governing protrusion length during twisting.

FEM results consistently show that the final protrusion length is primarily controlled by axial material feeding from the straight hairpin segment into the curved region during twisting. This feeding process is driven mainly by the twisting angle and the initial insertion length into the twisting tool, as illustrated by the deformation characteristics in Fig. 6. Based on this observation, the protrusion length $\mathrm{L_p}$ is expressed as a function of twisting-related kinematic variables as

$$\mathrm{L_p} = a_0 + a_1\theta + a_2 l_{ins} + a_3\theta l_{ins} \tag{1}$$

where θ denotes the twisting angle and l_{ins} represents the initial insertion length into the twisting tool. The coefficients a_i are regression parameters reflecting the effective geometric contribution of each term.

Eq. 1 is constructed to reflect the observed deformation mechanism rather than to maximize statistical fitting accuracy. The inclusion of the interaction term θl_{ins} accounts for the coupled effect of rotation and axial engagement, which governs the amount of material redistributed into the curved region during twisting. Other process variables were omitted because their direct effect on protrusion length was found to be limited within the feasible forming window.

Discussion

The FE results clarify the distinct roles of the expanding and twisting stages in determining the final protrusion length. Twisting governs the axial redistribution of material, where the straight segment is progressively fed into the curved region through coupled rotation and axial motion (Fig. 6). Consequently, the final protrusion is highly sensitive to the effective axial feed generated during twisting, making this stage the primary deformation-driving mechanism. In contrast, expanding mainly influences the local opening geometry and the stability of tool engagement. Once stable engagement is achieved, the direct impact of expanding on the final protrusion remains limited, and expanding can be regarded primarily as a feasibility-enabling step that provides physically realistic initial conditions for twisting.

Importantly, the observed layer-to-layer scatter in protrusion length cannot be explained by differences in twisting conditions, since identical forming settings are applied to all layers in production. Instead, simulations indicate that non-uniform initial protrusion lengths among layers are largely transmitted through the forming sequence, leading to a near one-to-one correspondence between the initial and final protrusion lengths. These findings suggest that protrusion variability arises from the combination of twisting-driven material redistribution and layer-dependent initial geometric offsets. The mechanistic understanding obtained here supports the development of reduced-order predictors for rapid estimation and motivates further investigation into geometry-based strategies for mitigating layer-to-layer variation.

Conclusion

This study presented an integrated FE framework to analyze protrusion variation in twisted hairpin legs by combining bilayer material modeling with mechanically consistent boundary conditions reconstructed from manufacturing observations. The framework enables systematic evaluation of the expanding and twisting stages while maintaining fidelity to the practical forming sequence.

The results indicate that twisting governs the final protrusion length through axial material redistribution from the straight segment into the curved region, whereas expanding mainly serves as a feasibility-enabling step that establishes stable tool engagement and provides physically realistic initial conditions for twisting. Furthermore, under production conditions where identical forming settings are applied across layers, the analysis demonstrates that layer-to-layer protrusion scatter is primarily driven by non-uniform initial protrusion geometry.

By clarifying the respective contributions of deformation-driven mechanisms and initial geometric offsets, this work provides a mechanistic basis for reduced-order prediction of protrusion behavior and motivates further development toward geometry-based variability control.

References

[1] W. Maddumage, S. Ouenzerfi, S. Harmand, A. Cairns, A. Paykani, Thermal management of hairpin winding traction motors in electric vehicles: Parametric evaluation of impinging oil jet cooling using CFD simulations, Appl. Therm. Eng. 273 (2025) 126414.

[2] A. Dannier, F. Di Bruno, F. Fiume, E. Fedele, G. Brando, Hairpin Winding Technology for Electric Traction Motors: Design, Prototyping, and Connection Rules, Proc. 2022 International Conference on Electrical Machines (ICEM), IEEE, pp. 1170–1175.

[3] H. Yu, L. Li, J. Wu, Laser welding method and quality analysis of hairpin windings in electric drive motors, Opt. Laser Technol. 174 (2024) 110452.

[4] T. Will, A. Olowinsky, M. Gillner, Prediction of electrical resistance of laser-welded copper pin-pairs with surface topographical information from inline post-process observation by optical coherence tomography, Int. J. Adv. Manuf. Technol. 127 (2023) 2947–2961.

[5] H. Choi, P. Fazily, J. Park, Y. Kim, J.H. Cho, J. Kim, J.W. Yoon, Artificial intelligence for springback compensation with electric vehicle motor component, Int. J. Mater. Form. 15 (3) (2022) 22.

[6] X. Long, X. Liu, H. Zhang, Indentation reverse algorithm of mechanical response for metallic coatings based on neural network and finite element method, Materials 16 (7) (2023) 2617.

[7] A.R. Hosseinzadeh, F. Berto, G. Meneghetti, Determination of mechanical properties using sharp macro-indentation test and inverse analysis, Theor. Appl. Fract. Mech. 89 (2017) 1–10.

[8] B.B. An, R.R. Wang, D.S. Zhang, Region-dependent micro damage of enamel under indentation, Acta Mech. Sin. 28 (6) (2012) 1651–1658.

[9] Z. Wang, K. Wang, W. Xu, X. Gong, F. Zhang, Mapping the mechanical gradient of human dentin–enamel junction at different intratooth locations, Dent. Mater. 34 (3) (2018) 376–388.

[10] I.N. Chou, S.C. Wang, Finite element analysis and optimization of springback reduction in U-channel bending, J. Mater. Process. Technol. 89–90 (1999) 340–347.

[11] N.A. Maske, J.K. Sawale, Taguchi approach for investigation of springback effect in aluminum sheet, Int. J. Mech. Eng. Rob. Res. 2 (3) (2013) 322–329.

[12] D.T. Nguyen, J.E. Park, D.H. Kim, Optimization of influential process parameters on the deep drawing of aluminium 6061 sheet using Taguchi method and finite element analysis, in: Proc. KSME Spring Conf., 2009, pp. 1045–1050.

[13] C. Depoorter, K. Faes, J. Penning, Mechanical heterogeneity in drawn copper wires due to microstructural gradients, Mater. Sci. Eng. A 666 (2016) 229–238.

[14] S.H. Choi, Y.S. Kim, J.W. Lee, Effect of drawing sequences on mechanical inconsistency in copper conductors, J. Mater. Process. Technol. 265 (2019) 1–10.

[15] N.V. Nguyen, J.J. Kim, S.E. Kim, Methodology to extract constitutive equation at a strain rate level from indentation curves, Int. J. Mech. Sci. 152 (2019) 363–377.